Theoretical Analysis of 630-nm Band GaInP–AlGaInP Strained Quantum-Well Lasers Considering Continuum States

Shun Tung Yen and Chien-Ping Lee, *Senior Member, IEEE*

***Abstract*— GaInP–AlGaInP strained quantum-well lasers with emission wavelength at 630-nm band are theoretically analyzed in detail and then optimized. The valence band structure of quantum wells is obtained by evaluating the 6×6 Luttinger–Kohn Hamiltonian including the coupling among the heavy hole, the light hole, and the spin-orbital split-off hole bands. The effect of optical transition from/to continuum states not confined to the quantum well is studied. It is found that the optical transition from/to the continuum states is serious as the band gap of the confining layers is close to the quasi-Fermi level separation, leading to considerable radiative current. This radiative current is undesirable since the corresponding optical transition does not contribute significantly to the threshold gain. The gain-radiative current characteristic is therefore poor for confining layers containing a low Al content. To avoid unreasonable gain/absorption, the non-Markovian convolution lineshape is used instead of the conventional Lorentzian lineshape. The leakage current is high for single quantum-well lasers with wide bandgap confining layers. It can be reduced by increasing the quantum-well number, the dopant concentration, and the band gap of cladding layers. The calculated threshold current agrees well with the observation. The band gap shrinkage due to the carrier-carrier interaction is considered to obtain an emission wavelength consistent with the experimental result.**

***Index Terms*— Quantum well lasers, quantum wells, semiconductor device modeling, semiconductor lasers, spontaneous emission, visible lasers.**

I. Introduction

THERE have been growing interests in GaInP–AlGaInP strained quantum-well (QW) lasers emitting at 630-nm band as a light source for optical-disk memory system, laser printers, bar-code readers, and pointers, and as a replacement for He–Ne lasers. However, this kind of lasers generally has a high threshold current. The leakage current is serious due to the inherent limit of band gap for this material system. It is therefore important to comprehend the laser characteristics and then to optimize the laser structure. The laser performance depends on the strain and the thickness of the QW, the material and the thickness of the confining layers, the dopant concentration and the material of the cladding layers, and so on. It has been demonstrated that introducing $\sim$0.7% tensile strain into the QW can effectively improve the threshold current for lasers with 633-nm emission wavelength [1]–[3]. Reduced threshold current has been achieved by using a highly doped p-cladding layer [4]–[6] and AlInP cladding layers [7], [8]. There have been several works on theoretical analysis of the lasers [3], [6], [9]–[11]. The attentions were mainly focused on the QW's and the cladding layers. However, the dependence of the laser performance on confining layers has not yet correctly analyzed.

The confining layers are generally designed to provide a tight confinement of optical mode. To obtain a large confinement factor, the refractive index and the thickness of the confining layers have to be properly chosen. If the refractive index is too low, the optical confinement will not be enough. But if the refractive index is too high, the required narrow bandgap will cause a high carrier concentration in the confining layers. Undesired electron-hole recombination in the confining layers may be therefore serious. In this paper, theoretical analysis of 630-nm GaInP–AlGaInP tensile-strained QW lasers is carried out. The effect of optical transition involving continuum states not confined to the QW is included. The 6×6 Luttinger–Kohn Hamiltonian containing deformation potentials is used for calculating the valence band structure of strained QW's [3], [10], [12], [13]. It considers the mixing of the heavy hole, the light hole, and the spin-orbital split-off hole bands. Since the transition from/to the continuum states is considered, the gain/absorption spectrum becomes sensitively dependent on the convolution lineshape function. The non-Markovian lineshap [14]–[16] is adopted to avoid an unreasonable gain/absorption which is obtained if the conventional Lorentzian lineshape is used. To obtain an emission wavelength consistent with the experiment, we consider the bandgap shrinkage due to the carrier-carrier interaction. The material parameters such as the Γ and X band gaps and the band offsets are taken from the newly reported data [11], [17], [18]. The gain and the radiative current are both divided into four components corresponding to the transitions: 1) from bound states to bound states, 2) from continuum states to bound states, 3) from bound states to continuum states, and 4) from continuum states to continuum states. The leakage current is taken into account and divided into the diffusion and the drift components to give a detailed interpretation of the leakage mechanism. We then investigate the gains, the radiative currents, the leakage currents, and the emission wavelength by varying the bandgap and the thickness

Manuscript received August 6, 1996; revised October 31, 1996. This work was supported by the National Science Council of the Republic of China under Contract NSC86-2215-E009-010.

The authors are with the Department of Electronics Engineering, National Chiao Tung University, Hsinchu, Taiwan, Republic of China.

Publisher Item Identifier S 0018-9197(97)01574-1.

of the confining layers for different QW numbers. The effects of the dopant concentration and the bandgap of the cladding layers on the laser performance are also studied. The structures are then optimized for single and double QW lasers.

This paper is organized as follows. In the next section, we present the theory used for calculating the band structures, the gains, the radiative currents, and the leakage currents. The calculated results and their interpretation are discussed in Section III. In the final section, the conclusion is drawn.

II. Theory

We consider GaInP–AlGaInP strained QW lasers with a conventional step separate-confinement heterostructure (SCH). The total current of the laser is assumed to be composed of two components: the radiative current and the leakage current. The nonradiative Auger recombination current is neglected. This is justified for this wide bandgap material system where the small split-off energy suppresses the Auger recombination. Only the electron leakage current over the p-cladding layer is considered since it is much larger than the hole leakage current over the n-cladding layer.

In calculating the threshold condition, we consider the gains or losses due to: 1) the bound-to-bound ($b \to b$), 2) the bound-to-continuum ($b \to c$), 3) the continuum-to-bound ($c \to b$), and 4) the continuum-to-continuum ($c \to c$) transitions in the waveguide region. The threshold condition is written as

$$\Gamma_{\rm QW}(g_{b\to b}+g_{b\to c}+g_{c\to b})+\Gamma_{\rm WG}g_{c\to c}=\alpha_i+\alpha_m \quad (1)$$

where $g_{b\to b}$, $g_{b\to c}$, $g_{c\to b}$, and $g_{c\to c}$ are the gain coefficients arising from the four different transitions. α_i is the internal loss due to other loss mechanisms and α_m is the mirror loss. $\Gamma_{\rm QW}$ is the optical confinement factor of the QW region. (For multiquantum well lasers, the QW region also includes the barriers between the wells.) $\Gamma_{\rm WG}$ is the confinement factor of the waveguide region which is defined here to be composed of the confining layers and the QW region. Since the gains are functions of the quasi-Fermi levels for the conduction and the valence bands, the quasi-Fermi levels can be found by solving the threshold condition (1). Once the quasi-Fermi levels are found, one can calculate the four components of the radiative current due to the four kinds of transitions. Since the electric field in the cladding layer depends on the majority carrier flow which supplies the radiative recombination current in the waveguide region, one can calculate the drift leakage current only after the total radiative current is obtained.

A. Bound Subband Structures

The $k\cdot p$ method is used to calculate the band structures. For the valence subbands bound in the QW's, we use the 6×6 Luttinger–Kohn Hamiltonian which includes the coupling among the six hole bands [3], [10], [12], [13]. The strain effect is also included in the Hamiltonian. It is necessary to consider the spin-orbital split-off bands for accurate band structures since the split-off energy is small for the wide gap material considered here. Under the axial approximation and assuming the layers are grown along the [001] direction (z axis), the 6×6 Luttinger–Kohn Hamiltonian is block-diagonalized into two 3×3 blocks [12], [13]:

$$H^v=\begin{bmatrix} H^U_{3\times3} & 0 \\ 0 & H^L_{3\times3}\end{bmatrix} \quad (2)$$

where

$$H^\sigma_{3\times3}=-\begin{bmatrix} P+Q-\Gamma_{8v} & R_k\mp iS_k & \sqrt{2}R_k\pm\frac{i}{\sqrt{2}}S_k \\ R_k\pm iS_k & P-Q-\Gamma_{8v} & \sqrt{2}Q\pm i\sqrt{\frac{3}{2}}S_k \\ \sqrt{2}R_k\mp\frac{i}{\sqrt{2}}S_k & \sqrt{2}Q\mp i\sqrt{\frac{3}{2}}S_k & P-\Gamma_{7v}\end{bmatrix} \quad (3)$$

$$\begin{aligned} P&=P_k+P_\varepsilon \\ Q&=Q_k+Q_\varepsilon \\ P_k&=\frac{\hbar^2}{2m_0}\left(\gamma_1k_t^2-\frac{\partial}{\partial z}\gamma_1\frac{\partial}{\partial z}\right) \\ Q_k&=\frac{\hbar^2}{2m_0}\left(\gamma_2k_t^2+2\frac{\partial}{\partial z}\gamma_2\frac{\partial}{\partial z}\right) \\ R_k&=\frac{\hbar^2}{2m_0}\frac{\sqrt{3}}{2}(\gamma_2+\gamma_3)k_t^2 \\ S_k&=-i\frac{\hbar^2}{2m_0}\sqrt{3}k_t\left(\frac{\partial}{\partial z}\gamma_3+\gamma_3\frac{\partial}{\partial z}\right) \\ P_\varepsilon&=-a_v(\varepsilon_{xx}+\varepsilon_{yy}+\varepsilon_{zz}) \\ Q_\varepsilon&=-\frac{b}{2}(\varepsilon_{xx}+\varepsilon_{yy}-2\varepsilon_{zz}). \end{aligned} \quad (4)$$

$\sigma=U$ (or L) is the index for the two 3×3 blocks. The upper (or lower) signs in (3) are for $\sigma=U$ (or L). Γ_{8v} and Γ_{7v} are the unstrained valence band edges. The split-off energy Δ is therefore equal to $\Gamma_{8v}-\Gamma_{7v}$. $k_t=(k_x^2+k_y^2)^{1/2}$. γ_1, γ_2, and γ_3 are the Luttinger parameters. a_v is the hydrostatic deformation potential of the valence band and b is the shear deformation potential. ε_{xx}, ε_{yy}, and ε_{zz} are the diagonal elements of the strain tensor and are given by

$$\begin{aligned} \varepsilon_{xx}&=\varepsilon_{yy}=\frac{a_0-a}{a} \\ \varepsilon_{zz}&=-\frac{2C_{12}}{C_{11}}\varepsilon_{xx}. \end{aligned} \quad (5)$$

a and a_0 are the lattice constants of the strained layer material and the substrate, respectively. C_{11} and C_{12} are the elastic stiffness constants.

The wave function in the valence bands can be expressed as

$$\Psi^{v\sigma}_{mk_t}(\mathbf{r})=\frac{e^{i\mathbf{k}_t\cdot\mathbf{r}_t}}{\sqrt{A}}\sum_{\nu=1,2,3}\psi^{v\sigma}_{m\nu k_t}(z)|\sigma,\nu\rangle \quad (6)$$

where $\psi^{v\sigma}_{m\nu k_t}(z)$ are the envelope functions, m is the subband index, A is the area of the QW, $\mathbf{k}_t=\hat{x}k_x+\hat{y}k_y$, and $\mathbf{r}_t=\hat{x}x+\hat{y}y\cdot|\sigma,\nu\rangle$ are the new transformed Bloch functions given by [12], [13]

$$\begin{aligned} |\sigma,1\rangle&=\frac{1}{2}\left[-|(X+iY)\uparrow\rangle e^{-i\frac{3}{2}\phi}\mp i|(X-iY)\downarrow\rangle e^{i\frac{3}{2}\phi}\right] \\ |\sigma,2\rangle&=\frac{1}{2\sqrt{3}}\left[-|(X-iY)\uparrow+2Z\downarrow\rangle e^{i\frac{1}{2}\phi}\right. \\ &\qquad\left.\pm i|-(X+iY)\downarrow+2Z\uparrow\rangle e^{-i\frac{1}{2}\phi}\right] \end{aligned}$$

$$|\sigma,3\rangle = \frac{1}{\sqrt{6}}\left[-|(X-iY)\uparrow - Z\downarrow\rangle e^{i\frac{1}{2}\phi} \mp i|(X+iY)\downarrow + Z\uparrow\rangle e^{-i\frac{1}{2}\phi}\right] \quad (7)$$

where $\phi = \tan^{-1}(k_y/k_x)$ and $\sigma = U$ (or L) for the upper (lower) signs. The subband energy dispersion and the envelope functions can then be obtained by solving the effective-mass equation

$$\sum_{\nu} H^{\sigma}_{3\times 3,\mu\nu}\psi^{v\sigma}_{m\nu k_t}(z) = E^{v\sigma}_{mk_t}\psi^{v\sigma}_{m\mu k_t}(z). \quad (8)$$

If the spatial varying potential has reflection symmetry, then $H^{U}_{3\times 3}(-z) = H^{L}_{3\times 3}(z)$, $E^{vU}_{mk_t} = E^{vL}_{mk_t}$, and $\psi^{vU}_{m\mu k_t}(-z) = \psi^{vL}_{m\nu k_t}(z)$.

To obtain the energy dispersion and the wave functions of the conduction band, we solve the one-band effective-mass equation

$$\left[\frac{\hbar^2}{2}\left(\frac{k_t^2}{m_{ct}} - \frac{\partial}{\partial z}\frac{1}{m_{cz}}\frac{\partial}{\partial z}\right) + V_c + a_c(\varepsilon_{xx}+\varepsilon_{yy}+\varepsilon_{zz})\phi^c_{nk_t}(z)\right] = E^c_{nk_t}\phi^c_{nk_t}(z) \quad (9)$$

where m_{ct} and m_{cz} are the electron effective masses in the x-y plane and in the z direction, respectively, V_c is the unstrained conduction band edge, a_c is the hydrostatic potential of the conduction band, $\phi^c_{nk_t}(z)$ is the envelope function, and n is the subband index. If the transverse effective mass m_{ct} is weakly dependent on z or the envelope function is tightly bound in the well, the solution of (9) can further approximate to

$$\phi^c_{nk_t}(z) \approx \phi^c_{nk_t=0}(z), \qquad E^c_{nk_t} \approx E^c_{nk_t=0} + \frac{\hbar^2 k_t^2}{2m_{ct}}. \quad (10)$$

The actual electron wave function is

$$\Phi^{c\eta}_{nk_t}(\mathbf{r}) = \frac{e^{i\mathbf{k}_t\cdot\mathbf{r}_t}}{\sqrt{A}}\phi^c_{nk_t}(z)|S_\eta\rangle \quad (11)$$

where η is the spin index which can be either $\uparrow$ or $\downarrow$. $|S\uparrow\rangle$ and $|S\downarrow\rangle$ are the Bloch functions at Γ_{6c} for spin up and spin down, respectively.

B. Continuum States Above the Barriers

The spontaneous emission due to optical transitions involving continuum states above the barriers is sometimes important. It is however not easy to include this effect in theoretical analysis. When a laser is at threshold, the band profile around the active region is nearly flat [19], [20]. This situation is illustrated in Fig. 1. Because one side of the system is open, the states with z-component energy higher than the barrier are continuum. To make the problem solvable, one can impose a fictitious infinite potential barrier on the open side which is far away from the active region. In this case, the states become discrete but the problem is still cumbersome. For a large bound domain, a large number of subbands have to be treated. The computation can be further simplified by changing the asymmetric potential profile in Fig. 1(a) to a symmetric one in Fig. 1(b). This model has been used in calculating the bound-to-free intersubband transition [21]. Due to the reflection symmetry of the potential, the envelope wave functions now have clear parity and one needs only to perform the overlap integral of envelope wave functions with the same parity.

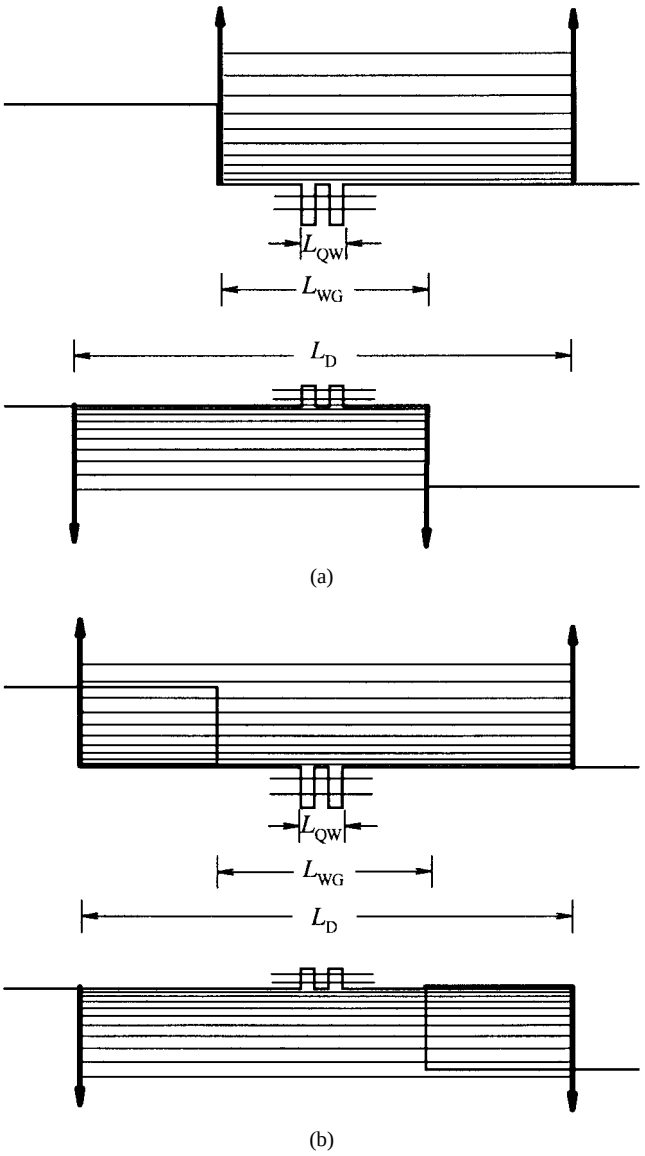

Fig. 1. The illustration for band profile at threshold. (a) Fictitious infinite potentials are imposed at the two boundaries for discretizing the continuum states. (b) The potential profile is modified to be symmetric.

Note that the discrete states in the Fig. 1(b) model are used only for the carriers in the waveguide region but not for the carriers in the cladding layers. The use of the discrete states in Fig. 1(b) to replace the continuum states is reasonable if the domain size L_D is large enough. In the calculation, the domain size is chosen to be large enough to make sure that the discrete states are dense enough to resemble the continuum states. In this situation, the physical quantities of the bound system are close to those of the open system. Furthermore, for a large L_D, the physical quantities of the bound system should not significantly depend on whether the system is symmetric or not. In other word, the physical quantities of the

symmetric system should be close to those of the asymmetric one. However, as will be shown later, the computation for the former is much easier than that for the latter.

For continuum states in the conduction band, the approximation (10) is also used. The electron wave functions can also be expressed in the form of (11). In the following, we will denote the envelope wave function as $\bar{\phi}^c_{nk_t}(z)$ and the eigenenergy as $\bar{E}^c_{nk_t}$ using the bar for continuum states to avoid confusion with the bound states.

For continuum states in the valence band, we neglect the band coupling. Only the diagonal elements of the effective Hamiltonian $H^\sigma_{3\times3}$ in (3) are used:

$$\bar{H}^\sigma_{3\times3} = -\begin{bmatrix} P+Q-\Gamma_{8v} & 0 & 0 \\ 0 & P-Q-\Gamma_{8v} & 0 \\ 0 & 0 & P-\Gamma_{7v} \end{bmatrix}. \tag{12}$$

The effective mass equation is decoupled to three one-band effective-mass equations for the heavy hole, the light hole, and the spin-orbital split-off hole bands. The parabolic approximation similar to (10) is also used to obtain the envelope functions and the energy dispersion of each band. The wave functions are no longer mixed and can be expressed as

$$\bar{\Psi}^{v\sigma}_{m\nu k_t}(\mathbf{r}) = \frac{e^{i\mathbf{k}_t\cdot\mathbf{r}_t}}{\sqrt{A}}\bar{\psi}^{v\sigma}_{m\nu k_t}(z)\,|\,(\sigma,\nu)'\rangle \quad \text{for } \nu = 1,2,\text{and } 3 \tag{13}$$

with the eigenenergy of $\bar{E}^{v\sigma}_{m\nu k_t}$, where $|(\sigma,\nu)'\rangle$ is the rotated cell-periodic function defined in the Appendix. Because $\bar{H}^U_{3\times3} = \bar{H}^L_{3\times3}$, we have $\bar{E}^{vU}_{m\nu k_t} = \bar{E}^{vL}_{m\nu k_t}$ and $\bar{\psi}^{vU}_{m\nu k_t}(z) = \bar{\psi}^{vL}_{m\nu k_t}(z)$.

C. Carrier Density and Quasi-Fermi Level

In the calculation, we assume that the electrons in the conduction bands (including the Γ and the X valleys) and the holes in the valence bands (including various hole bands) reach their own quasi-equilibrium condition. The carrier distribution satisfies the Fermi–Dirac distribution in each band and can be determined by the corresponding quasi-Fermi level. This is a good approximation in calculating the threshold current of a laser in which the stimulated emission is not significant.

Because the gain coefficients are functions of two variables, the quasi-Fermi levels of the conduction, and the valence bands, it requires an additional condition to solve the threshold condition (1). Assuming the active region is undoped and the charge neutrality condition holds in the QW region, we have

$$n_{\rm QW} = p_{\rm QW} \tag{14}$$

where

$$n_{\rm QW} = n^\Gamma_{\rm bound} + n^\Gamma_{\rm conti} + n^X_{\rm QW} \tag{15}$$

is the electron density in the QW region and

$$p_{\rm QW} = p_{\rm bound} + p_{\rm conti} \tag{16}$$

is the hole density in the QW region. $n^\Gamma_{\rm bound}$ and $n^\Gamma_{\rm conti}$ are the densities of Γ electrons in the bound states and the continuum states, respectively. $n^X_{\rm QW}$ is the density of electrons which populate the X valleys in the QW region. $p_{\rm bound}$ and $p_{\rm conti}$ are the densities of holes in the bound states and the continuum states, respectively. These carrier densities can be related to their corresponding quasi-Fermi levels, $E_{\rm fc}$ or $E_{\rm fv}$ [22].

D. Optical Gain and Momentum Matrix Element

The optical gain is calculated based on the standard time-dependent perturbation theory (the Fermi's Golden Rule). Including the effect of lifetime broadening, the gain coefficients for transitions to bound valence states, $g_{b\to b}$ and $g_{c\to b}$, can be written as [13]

$$g(\hbar\omega) = \frac{\pi q^2}{n_r c\varepsilon_0 m_0^2 \omega L_{\rm QW}} \sum_{\eta=\uparrow,\downarrow}\sum_{\sigma=U,L}\sum_{n,m}\int \left|\hat{e}\cdot\mathbf{M}^{\eta\sigma}_{nm}(k_t)\right|^2 \times \left(f^c_{nk_t} - f^{v\sigma}_{mk_t}\right) L\left(\hbar\omega - E^{cv\sigma}_{nmk_t} - \Delta_{cv}\right)\frac{k_t}{2\pi}dk_t \tag{17}$$

where q is the electronic charge, m_0, c, and ε_0 are the electron mass, the velocity of light, and the permittivity in free space, respectively, and n_r is the refractive index averaged over the QW region. $L_{\rm QW}$ is the width of the QW region. $f^c_{nk_t}$ and $f^{v\sigma}_{mk_t}$ are the occupation probabilities for *electrons* in the conduction and the valence bands, respectively. $L(\hbar\omega - E^{cv\sigma}_{nmk_t} - \Delta_{cv})$ is the broadening lineshape function for the inclusion of intraband relaxation effects and will be discussed in the following subsection.

$$E^{cv\sigma}_{nmk_t} = E^c_{nk_t} - E^{v\sigma}_{mk_t} \tag{18}$$

is the transition energy and Δ_{cv} is the carrier-density-dependent bandgap shrinkage energy. $\mathbf{M}^{\eta\sigma}_{nm}(k_t) = \langle\Psi^{v\sigma}_{mk_t}|\mathbf{p}|\Phi^{c\eta}_{nk_t}\rangle$ is the momentum matrix element and $\hat{e}$ is the polarization vector. Using the wave functions in (6) and (11), one can obtain the TE and TM squared momentum matrix elements [13]:

$$\begin{aligned}|M_{\rm TE}|^2 &= \left|\hat{x}\cdot\mathbf{M}^{\eta\sigma}_{nm}(k_t)\right|^2 = \left|\hat{y}\cdot\mathbf{M}^{\eta\sigma}_{nm}(k_t)\right|^2 \\ &= \frac{M_b^2}{4}\Big[3\left|\langle\psi^{v\sigma}_{m,\nu=1,k_t}\mid\phi^c_{nk_t}\rangle\right|^2 \\ &\qquad + \left|\langle\psi^{v\sigma}_{m,\nu=2,k_t} + \sqrt{2}\psi^{v\sigma}_{m,\nu=3,k_t}\mid\phi^c_{nk_t}\rangle\right|^2\Big]\end{aligned} \tag{19}$$

and

$$\begin{aligned}|M_{\rm TM}|^2 &= \left|\hat{z}\cdot\mathbf{M}^{\eta\sigma}_{nm}(k_t)\right|^2 \\ &= M_b^2\left|\langle\psi^{v\sigma}_{m,\nu=2,k_t} - \frac{1}{\sqrt{2}}\psi^{v\sigma}_{m,\nu=3,k_t}\mid\phi^c_{nk_t}\rangle\right|^2\end{aligned} \tag{20}$$

with the average bulk momentum matrix element

$$M_b^2 = \frac{1}{3}|\langle S|p_x|X\rangle| = \frac{1}{6}m_0E_p \tag{21}$$

where E_p is the Kane's energy parameter. For structures with reflection symmetry, we have the properties of $\psi^{vU}_{m\nu k_t}(-z) = \psi^{vL}_{m\nu k_t}(z)$, $E^{vU}_{mk_t} = E^{vL}_{mk_t}$, and $\phi^c_{nk_t}$ having a clear parity. This makes $|M_{\rm TE}|^2$ and $|M_{\rm TM}|^2$ independent of the indexes η and σ. The summations over η and σ in (17) can thus be replaced by the factor 4, implying that we need to treat only one of the two 3×3 blocks when calculating the optical gain. This is

why we use the symmetric potential in Fig. 1(b) to calculate the continuum states.

For the $b \rightarrow c$ transition, the optical gain $g_{b\rightarrow c}$ can be written as

$$g_{b\rightarrow c}(\hbar\omega) = \frac{\pi q^2}{n_r c\varepsilon_0 m_0^2 \omega L_{\mathrm{QW}}} 4 \sum_{v=1,2,3} \sum_{n,m} \int \left|\hat{e}\cdot \mathbf{M}_{nmv}^{\eta\sigma}(k_t)\right|^2 \times \left(f_{nk_t}^{c} - f_{m\nu k_t}^{v\sigma}\right) L\left(\hbar\omega - E_{nm\nu k_t}^{cv\sigma} - \Delta_{cv}\right) \frac{k_t}{2\pi} dk_t \tag{22}$$

where the electron occupation probability in the valence bands $f_{m\nu k_t}^{v\sigma}$ and the transition energy $E_{nm\nu k_t}^{cv\sigma}$ have the same definitions described earlier except that the bound state energy $E_{mk_t}^{v\sigma}$ is replaced by the continuum state energy $\bar{E}_{m\nu k_t}^{v\sigma}$. For the momentum matrix elements $\mathbf{M}_{nm\nu}^{\eta\sigma}(k_t) = \langle \bar{\Psi}_{m\nu k_t}^{v\sigma} | \mathbf{p} | \Phi_{nk_t}^{c\eta} \rangle$, we use the polarization dependent formula [22]–[25] (see the Appendix):

$$|M_{\mathrm{TE},\nu=1}|^2 = \left|\hat{x}\cdot \mathbf{M}_{nm,\nu=1}^{\eta\sigma}(k_t)\right|^2 = \left|\hat{y}\cdot \mathbf{M}_{nm,\nu=1}^{\eta\sigma}(k_t)\right|^2 = \frac{3}{8} M_b^2 (1+\cos^2\theta) \left|\left\langle \bar{\psi}_{m,\nu=1,k_t}^{v\sigma} \mid \phi_{nk_t}^{c} \right\rangle\right|^2 \tag{23}$$

$$|M_{\mathrm{TE},\nu=2}|^2 = \frac{1}{8} M_b^2 (5-\cos^2\theta) \left|\left\langle \bar{\psi}_{m,\nu=2,k_t}^{v\sigma} \mid \phi_{nk_t}^{c} \right\rangle\right|^2 \tag{24}$$

$$|M_{\mathrm{TE},\nu=3}|^2 = \frac{1}{2} M_b^2 \left|\left\langle \bar{\psi}_{m,\nu=3,k_t}^{v\sigma} \mid \phi_{nk_t}^{c} \right\rangle\right|^2 \tag{25}$$

for TE polarization waves and

$$|M_{\mathrm{TM},\nu=1}|^2 = \left|\hat{z}\cdot \mathbf{M}_{nm,\nu=1}^{\eta\sigma}(k_t)\right|^2 = \frac{3}{4} M_b^2 (1-\cos^2\theta) \left|\left\langle \bar{\psi}_{m,\nu=1,k_t}^{v\sigma} \mid \phi_{nk_t}^{c} \right\rangle\right|^2 \tag{26}$$

$$|M_{\mathrm{TM},\nu=2}|^2 = \frac{1}{4} M_b^2 (1+3\cos^2\theta) \left|\left\langle \bar{\psi}_{m,\nu=2,k_t}^{v\sigma} \mid \phi_{nk_t}^{c} \right\rangle\right|^2 \tag{27}$$

$$|M_{\mathrm{TM},\nu=3}|^2 = \frac{1}{2} M_b^2 \left|\left\langle \bar{\psi}_{m,\nu=3,k_t}^{v\sigma} \mid \phi_{nk_t}^{c} \right\rangle\right|^2 \tag{28}$$

for TM polarization waves, where $\theta = \cos^{-1}(k_z/k)$. Strictly speaking, there is no clearly defined k_z because k_z is not a good quantum number in the layer structure without translation symmetry in the z direction. However, a clear k_z can be found in each layer by using the one-band effective-mass equation (12). We average $\cos^2\theta$ of each layer over the QW region to obtain the squared momentum matrix element since the $b \rightarrow c$ transition mainly occurs in the QW region. Again, the squared momentum matrix elements here are independent of the indexes η and σ and we have replaced the summations over η and σ by 4 in (22).

For the $c \rightarrow c$ transition, the gain $g_{c\rightarrow c}$ can also be expressed as (22) but the integral of envelope wave functions in the momentum matrix element is carried out over the entire domain defined in Fig. 1(b) and the average length L_{QW} in (22) has to be changed to the entire domain size L_D. The $\cos^2\theta$ is here averaged over the waveguide region because the $c \rightarrow c$ transition occurs only in the waveguide region.

The TE and the TM gains are both calculated. The lasing mode and the emission wavelength are obtained when the carrier density reaches the threshold condition (1). The quasi-Fermi levels are then obtained by solving (1) and (14). We assume the quasi-Fermi levels are flat throughout a wide range. This assumption is valid and often used in calculation [22].

E. Lineshape Function

To include the effect of the intraband relaxation, a broadening lineshape function is generally used in the gain calculation. There have been many reports on the gain analysis using the Lorentzian lineshape function [3], [9]–[11], [13]. However, in spite of its simplicity, the Lorentzian lineshape may cause unnatural results. The slow decay of the lineshape in the long wavelength range may cause an unreasonably large absorption of photons with energy well below the bangap, inconsistent with the observed result. In this study, the choice of the lineshape function is especially important since the effect of the transition in the confining layers is included. A poorly chosen lineshape function will result in a large absorption loss in the confining layers. This problem can be avoided by using more accurate lineshapes by considering the non-Markovian process in the intraband relaxation [14]–[16]. It is, however, difficult to calculate the non-Markovian lineshape function from the first principle in device simulation. Fortunately, it is found that the non-Markovian lineshape can be well fitted by the simple form

$$L(E) = \frac{1}{N} \frac{\Gamma(E)}{E^2 + \Gamma^2(E)} \tag{29}$$

with

$$\Gamma(E) = C e^{K_1} e^{-K_2|E|} \tag{30}$$

where N is chosen so that the lineshape function $L(E)$ is normalized. Only three fitting parameters, C, K_1, and K_2, are needed. These parameters are functions of the carrier density, temperature, and the band structures. However, in the interesting range of carrier density and temperature for QW lasers, the lineshape is not sensitively dependent on these factors. So, in this study, we assume that the fitting parameters are all constant. Fig. 2 shows the non-Markovian lineshape with $C = 0.005$ eV, $K_1 = 10$ eV^{-1}, and $K_2 = 30$ eV^{-1} and the conventional Lorentzian lineshape with a 0.1-ps relaxation time. One can see that the non-Markovian lineshape has a low-energy tail steeper than the high-energy one. The unnatural low-energy absorption due to the Lorentzian lineshape can therefore be avoided.

Note that in (17) and (22), we have considered the bandgap shrinkage due to the carrier-carrier exchange. This effect causes red shift of the spectrum and is important to be included in order to obtain an emission wavelength consistent with the experiment. We use the 1/3-power formula for the bandgap shrinkage [22]:

$$\Delta_{cv} = -c \times 10^{-8} n_{\mathrm{QW}}^{1/3} \tag{31}$$

where c is chosen to be 3.2. This 1/3-power relation has been demonstrated to be valid at high carrier densities [26]–[28].

F. Radiative Recombination Current

We have considered four kinds of optical transitions which result in four gain coefficients. At the same time, the transitions

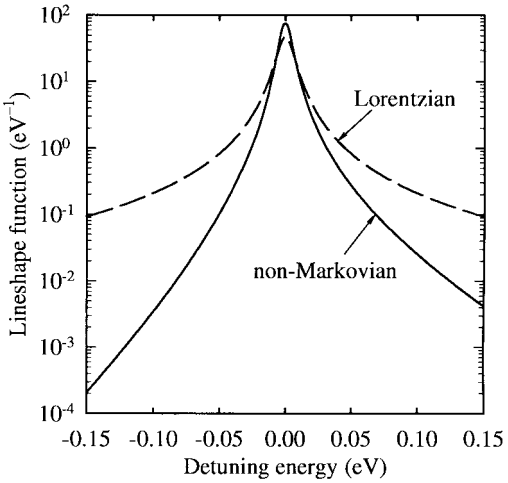

Fig. 2. The non-Markovian lineshape function (the solid line) with $C = 0.005$ eV, $K_1 = 10\ \text{eV}^{-1}$, and $K_2 = 30\ \text{eV}^{-1}$ and the Lorentzian lineshape function (the dashed line) with a 0.1-ps scattering time.

also cause radiative currents. The radiative current density is also composed of four components:

$$J_{\text{rad}} = J_{b\to b} + J_{b\to c} + J_{c\to b} + J_{c\to c}. \tag{32}$$

Each component of radiative current densities is calculated"

$$\begin{aligned} J_{b\to b} &= qL_{\text{QW}}R_{\text{sp},b\to b} \\ J_{c\to b} &= qL_{\text{QW}}R_{\text{sp},c\to b} \\ J_{b\to c} &= qL_{\text{QW}}R_{\text{sp},b\to c} \\ J_{c\to c} &= qL_{\text{QW}}R_{\text{sp},c\to c} \end{aligned} \tag{33}$$

where $R_{\text{sp},b\to b}, R_{\text{sp},c\to b}, R_{\text{sp},b\to c}$, and $R_{\text{sp},c\to c}$ are the spontaneous emission rates due to the four corresponding transitions and L_{WG} is the width of the waveguide region (see Fig. 1). Note that for $J_{b\to b}, J_{c\to b}$, and $J_{b\to c}$, the size of the QW region, L_{QW}, is used since the three recombination processes occur mainly in the QW region. However, for the $c \to c$ radiative current density $J_{c\to c}$, the recombination occurs throughout the waveguide region and we multiply $R_{\text{sp},c\to c}$ by L_{WG}. The spontaneous emission rates for transitions to bound states, $R_{\text{sp},b\to b}$ and $R_{\text{sp},c\to b}$, can be calculated by the formula

$$\begin{aligned} R_{\text{sp}} = \frac{q^2 n_r}{\pi\hbar^2 c^3 \varepsilon_0 m_0^2 L_{\text{QW}}} 4 \sum_{n,m} \int |M_{\text{sp}}(k_t)|^2 \\ \times f_{nk_t}^{c}\left(1 - f_{mk_t}^{v\sigma}\right) E_{nmk_t}^{cv\sigma} \frac{k_t}{2\pi} dk_t \end{aligned} \tag{34}$$

where the squared momentum matrix element of the spontaneous emission

$$\begin{aligned} |M_{\text{sp}}|^2 &= \frac{1}{3}\left(2|M_{\text{TE}}|^2 + |M_{\text{TM}}|^2\right) \\ &= \frac{1}{2} M_b^2 \sum_{\nu=1,2,3} \left|\left\langle \psi_{m\nu k_t}^{v\sigma} \mid \phi_{nk_t}^{c} \right\rangle\right|^2 \end{aligned} \tag{35}$$

is the average of two TE polarization components and one TM polarization component. Again, summations over η and σ have been replaced by 4 in formula (34). For the spontaneous emission rate $R_{\text{sp},c\to b}$, the formula is

$$\begin{aligned} R_{\text{sp},b\to c} = \frac{q^2 n_r}{\pi\hbar^2 c^3 \varepsilon_0 m_0^2 L_{\text{QW}}} 4 \sum_{\nu=1,2,3} \sum_{n,m} \int |M_{\text{sp},\nu}(k_t)|^2 \\ \times f_{nk_t}^{c}\left(1 - f_{m\nu k_t}^{v\sigma}\right) E_{nm\nu k_t}^{cv\sigma} \frac{k_t}{2\pi} dk_t \end{aligned} \tag{36}$$

where the squared momentum matrix elements of spontaneous emission

$$\begin{aligned} |M_{\text{sp},\nu}|^2 &= \frac{1}{3}\left(2|M_{\text{TE},\nu}|^2 + |M_{\text{TM},\nu}|^2\right) \\ &= \frac{1}{2} M_b^2 \left|\left\langle \psi_{m\nu k_t}^{v\sigma} \mid \phi_{nk_t}^{c} \right\rangle\right|^2 \end{aligned} \tag{37}$$

for $\nu = 1,\ 2$, and 3. The spontaneous emission rate $R_{\text{sp},c\to c}$ can be expressed by (36) except that L_{QW} is replaced by L_D and the integrals of the wave functions for momentum matrix elements are over the entire domain, similar to the case in the gain formula $g_{b\to b}$.

G. Leakage Current

The formulas for the leakage current are derived following the conventional method [22], [29]. The total current density is

$$J_{\text{total}} = J_{\text{rad}} + J_{\text{leakage}}. \tag{38}$$

The hole leakage current over the n-cladding layer is neglected. In the p-cladding layer, the total current density is

$$J_{\text{total}} = J_p + J_n = J_p + J_{\text{leakage}} \tag{39}$$

where J_p and J_n are the hole and the electron current densities in the p-cladding layer, respectively, and J_n is the same as J_{leakage}. Comparing (38) with (39), we have

$$J_{\text{rad}} = J_p \approx q\mu_p p_{\text{clad}} E \tag{40}$$

where μ_p is the hole mobility, p_{clad} is the hole density (near the waveguide region), and E is the electric field, respectively, in the p-cladding layer. The leakage current density is further divided into

$$J_{\text{leakage}} = J_n = J_{\text{drift}} + J_{\text{diffusion}} \tag{41}$$

where

$$J_{\text{drift}} = q\mu_n n_{\text{clad}} E = \frac{\mu_n}{\mu_p} \frac{n_{\text{clad}}}{p_{\text{clad}}} J_{\text{rad}} \tag{42}$$

is the drift current density and

$$\begin{aligned} J_{\text{diffusion}} = \frac{1}{2}\Bigg\{ -1 + \sqrt{1 + \left(\frac{2Z}{L_n}\right)^2} \\ \times \coth\left[\frac{W_p}{2Z}\sqrt{1 + \left(\frac{2Z}{L_n}\right)^2}\right]\Bigg\} J_{\text{drift}} \end{aligned} \tag{43}$$

is the diffusion current density. μ_n, n_{clad}, and L_n are the electron mobility, the electron density near the waveguide region, and the electron diffusion length, respectively, in the p-cladding layer. W_p is the thickness of the p-cladding layer, and Z is the effective field length defined as $Z = k_B T/qE$.

The carrier densities, $p_{\rm clad}$ and $n_{\rm clad}$, are calculated by using the quasi-Fermi level difference obtained from the previous calculation and requiring the charge neutrality in the cladding layer

$$p_{\rm clad} = n_{\rm clad} + N_A \tag{44}$$

where N_A is the doping concentration in the p-cladding layer, $n_{\rm clad}$ includes the electrons in the Γ and the X valleys, and $p_{\rm clad}$ contains holes in the split-off bands as well as in the heavy-hole and the light-hole bands.

H. Material Parameters

The material parameters of the AlGaInP system lattice-matched to GaAs are not as well known as those of the AlGaAs system. Recently, several measurements on this material system have given some reliable results [11], [17], [18], [30]–[34]. The material parameters used in this work are mainly taken from the data reported recently by Meney *et al.* [11], [17], [18]. The Γ and X bandgaps of $(Al_xGa_{1-x})_{0.5}In_{0.5}P$ at 300 K are given by

$$E_g^{\Gamma} = 1.900 + 0.610x \ (\text{eV}) \tag{45}$$

$$E_g^{X} = 2.204 + 0.085x \ (\text{eV}). \tag{46}$$

The band discontinuities for unstrained $Ga_yIn_{1-y}P$ in $(Al_xGa_{1-x})_{0.5}In_{0.5}P$ barrier are assumed to be

$$-\Delta E_v = -0.5\Delta E_g(y) - 0.063x - 0.157x^2 \ (\text{eV}) \tag{47}$$

$$\Delta E_c = 0.5\Delta E_g(y) + 0.574x - 0.157x^2 \ (\text{eV}) \tag{48}$$

where $\Delta E_g(y)$ is the bandgap difference between $Ga_{0.5}In_{0.5}P$ and $Ga_yIn_{1-y}P$:

$$\Delta E_g(y) = E_g(Ga_{0.5}In_{0.5}P) - E_g(Ga_yIn_{1-y}P) \tag{49}$$

and the bandgap of $Ga_yIn_{1-y}P$ is given by fitting to those of InP, $Ga_{0.5}In_{0.5}P$, and GaP. These data are considerably different from those reported in the earlier years [35]. However, as will be seen in the following section, our calculated results using the new parameters agree well with the measured results. The other parameters for $(Al_xGa_{1-x})_{0.5}In_{0.5}P$ used in the calculation are obtained by linear interpolation among InP, GaP, and AlP, which are listed in Table I. The refractive index for calculating optical modes is obtained from [35]. The mobilities of electrons and holes in the p-cladding layer are assumed to be $\mu_n = 100$ cm^2/V·s and $\mu_p = 10$ cm^2/V·s, respectively, and the electron diffusion length is $L_n = 0.6$ μm. In calculating the band structures of strained wells, we assume the deformation potential $a_c : -a_v = 3 : 1$.

TABLE I
MATERIAL PARAMETERS OF InP, GaP, AND AlP

Parameters	InP	GaP	AlP
E_p (eV)	20.4	22.2	17.7
Δ (eV)	0.108	0.08	0.07
γ_1	6.28	4.2	3.47
γ_2	2.08	0.98	0.06
γ_3	2.76	1.66	1.15
m_c^{Γ}/m_0	0.077	0.15	0.22
m_l^{X}/m_0	2.2	2.2	2.2
m_t^{X}/m_0	0.2	0.2	0.2
a_0 (Å)	5.8688	5.4512	5.4512
C_{11} (10^{11} dyne/cm^2)	10.22	14.12	13.2
C_{12} (10^{11} dyne/cm^2)	5.76	6.52	6.3
a_c–a_v (eV)	−6.4	−9.6	−8.7
b (eV)	−1.6	−1.5	−1.6

III. RESULTS AND DISCUSSION

In the section, we analyze the laser characteristics in detail by investigating the performance as a function of the confining layer thickness, the Al content of the confining layers, and the QW number. The laser structures are composed of 1-μm $(Al_{0.7}Ga_{0.3})_{0.5}In_{0.5}P$ cladding layers ($W_p = 1$ μm) and 80-Å $Ga_{0.6}In_{0.4}P$ tensile-strained QW's. The doping concentration in the p-cladding layer is 1×10^{18} cm^{-3} and that in the n-cladding layer is assumed to be sufficiently high so that the hole leakage current over the n-cladding layer can be neglected. The internal loss is assumed to be $\alpha_i = 10$ cm^{-1} and the cavity length is 500 μm long, leading to a mirror loss of $\alpha_m = 24$ cm^{-1}. The temperature is 300 K.

A. Single QW

In this subsection, single QW lasers are considered. Fig. 3 shows the TM peak gain versus the radiative current density for three different Al contents of the confining layer material $(Al_xGa_{1-x})_{0.5}In_{0.5}P$ ($x = 0.4, 0.5$, and 0.6). The confining layers are taken to be 100 nm. The TE peak gain is smaller than the TM peak gain for the tensile-strained lasers. As can be seen, the transparency current density is lower for lasers with a higher Al content in the confining layers. This is because a smaller number of carriers spill over the barriers when the Al content is high. On the other hand, when the confining layers have a low Al content, a large amount of spilled-over carriers cause a considerable radiative current which, as will be seen later, does not contribute to the TM gain efficiently. As a result, to reach the transparency condition, the radiative current is lower for the confining layers with a higher Al content. The spilled-over carriers also cause another disadvantage which can be clearly seen from Fig. 3 that the differential gain $(dg/dJ_{\rm rad})$ is poorer for devices with lower Al barriers. These results cannot be obtained without considering the recombination of the spilled-over carriers, or recombinations due to the optical transition from/to the continuum states. Note that the differential gain for $x = 0.6$ is poorer than for $x = 0.5$. This is because there is only a light-hole subband confined to the shallower QW $(x = 0.5)$ but there are two subbands (one light-hole and one heavy-hole subbands) confined to the deeper QW $(x = 0.6)$. Since the optical transition to the heavy-hole subband contributes nearly no TM gain, the differential gain is poorer for $x = 0.6$.

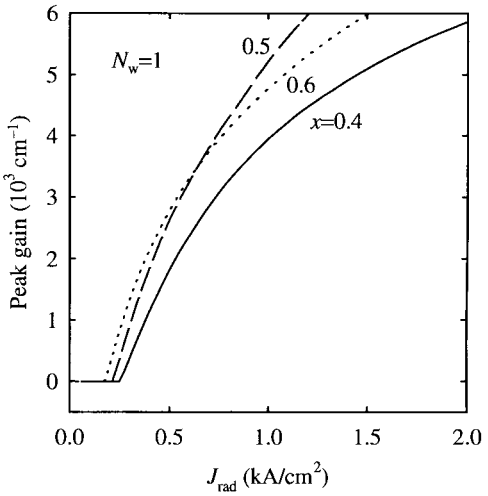

Fig. 3. The peak gain versus the radiative current density characteristic for single QW lasers.Three different Al contents of the $(Al_xGa_{1-x})_{0.5}In_{0.5}P$ confining layers are considered, $x = 0.4,\ 0.5$, and 0.6.

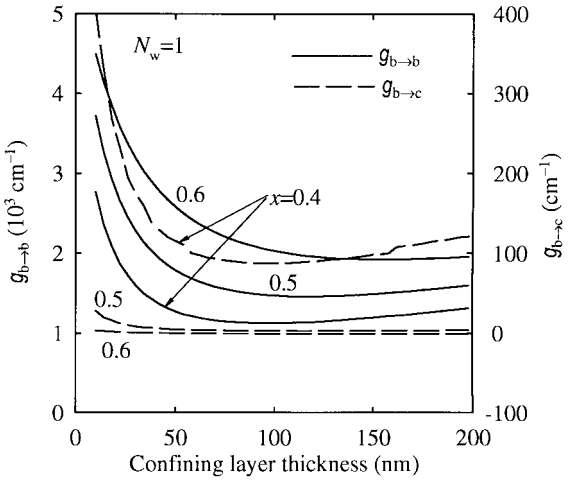

Fig. 4. The bound-to-bound gain g_{b-b} (the solid lines) and the bound-to-continuum gain g_{b-c} (the dashed lines) versus the thickness of confining layers for single QW lasers at threshold. Three different Al contents of the $(Al_xGa_{1-x})_{0.5}In_{0.5}P$ confining layers are considered, $x = 0.4,\ 0.5$, and 0.6.

Lasers with high-Al-content confining layers have a drawback. Because of the high Al content, the refractive index of the confining layers is closer to that of the cladding layers. It results in a small confinement factor. So a higher gain is needed for such devices to reach threshold. Since a larger quasi-Fermi level separation is required to obtain a higher gain, the leakage current over the cladding layers becomes higher.

To understand the properties of the lasers, it is necessary to analyze in detail the behaviors of the gain, the radiative current, the leakage current. Fig. 4 shows $g_{b\to b}$ and $g_{b\to c}$ at threshold versus the confining layer thickness for the three different Al contents in confining layers ($x = 0.4, 0.5$, and 0.6). One can see that $g_{b\to b}$ is higher when the confining layers are thinner. $g_{b\to b}$ is also higher for higher Al content in the confining layers. These are all caused by the reduction in the confinement factor as a result of such structure changes. One can find that a deep QW (with a high x in the confining layers) has a smaller $g_{b\to c}$. There are two reasons. First, for a deep well, the difference of the occupation probabilities, $f^c_{nk_t} - f^{v\sigma}_{m\nu k_t}$, is small. Secondly, the detuning energy $\hbar\omega - E^{cv\sigma}_{nm\nu k_t} - \Delta_{cv}$ is far apart from zero so that the gain $g_{b\to c}$ after convolved by the lineshape function becomes very small. As a result, for devices with high-Al confining layers (such as $x > 0.4$), $g_{b\to c}$ can be totally neglected. Even for those with low-Al confining layers, $g_{b\to c}$ is still very small compared to $g_{b\to b}$. The $c \to b$ gain $g_{c\to b}$ has a negative value and is much smaller than $g_{b\to c}$. The reason is because there are more holes in the continuum states than electrons in the continuum states due to the fact that the conduction-band QW is much deeper than the valence-band QW [see (47) and (48)]. The $c \to c$ gain $g_{c\to c}$ is the smallest of the four components of the gain because the transition energy $E^{cv\sigma}_{nm\nu k_t}$ is much higher than the emission energy $\hbar\omega$.

The gain coefficients mentioned above are all very dependent on the convolution lineshape function. We have calculated the gains using the conventional Lorentzian lineshape. Absorption larger than 100 cm^{-1} were obtained for both $g_{c\to b}$ and $g_{c\to c}$. This is in conflict with the experimental observation. The use of the non-Markovian lineshape function alleviates this problem and the results agree with the observation.

The radiative current densities $J_{b\to b}$ and $J_{b\to c}$ are shown in Fig. 5(a) as functions of the thickness of the confining layer and its Al content. Similar to the gain $g_{b\to b}$, higher Al contents or smaller thicknesses of the confining layers lead to higher $J_{b\to b}$. Unlike the behavior of $J_{b\to b}$, $J_{b\to c}$ is higher for devices with a lower Al content in the confining layers. The reason is similar to the case for $g_{b\to c}$, shown in Fig 4. However, different from $g_{b\to c}$, which is much smaller than $g_{b\to b}$, $J_{b\to c}$'s are comparable to $J_{b\to b}$'s. This difference is due to the lineshape function. The gain is very sensitive to the detuning energy of the convolution lineshape function but the total spontaneous emission rate is independent of the lineshape function. As a result, a small gain does not necessarily mean a low radiative current. Fig. 5(b) shows the $c \to c$ radiative current density $J_{c\to c}$ and the total radiative current density $J_{\rm rad}$. One can see that $J_{c\to c}$'s are almost linearly dependent on the confining layer thickness. This is because the $c \to c$ transition occurs throughout the whole waveguide region. To demonstrate the validity of our model, we have calculated the bimolecular recombination coefficient B by the empirical formula

$$J_{c\to c} = B n^{\Gamma}_{\rm conti} p_{\rm conti}. \tag{50}$$

We found that the coefficient B is 1.0$\sim$1.5$\times 10^{-10}$ cm^{3}s^{-1}, which is in excellent agreement with the experimental result [36]. The $c \to b$ radiative current $J_{c\to b}$ can be neglected compared with the other components of the radiative current since the $c \to b$ transition occurs only within the QW region and the factor $f^c_{nk_t}(1 - f^{v\sigma}_{mk_t})$ is small. Note that for devices with a shallow QW ($x = 0.4$), $J_{b\to c}$ and $J_{c\to c}$ are higher compared with those for devices with a deep QW. Since, as described above, $J_{b\to c}$ and $J_{c\to c}$ do not contribute very much to the gain, the gain-radiative current characteristics should be better for devices with deep wells. This is in agreement with the result shown in Fig. 3. It is noteworthy that lasers with

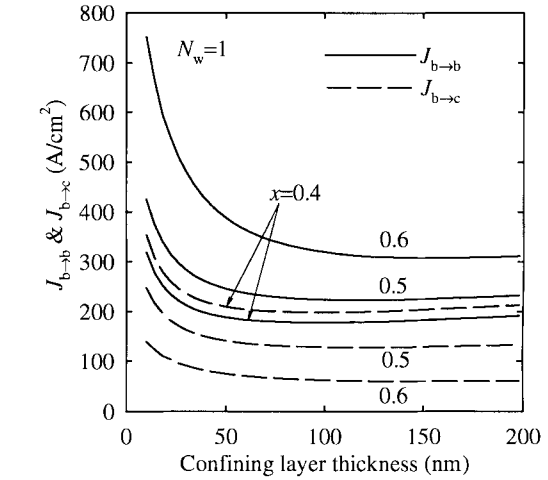

(a)

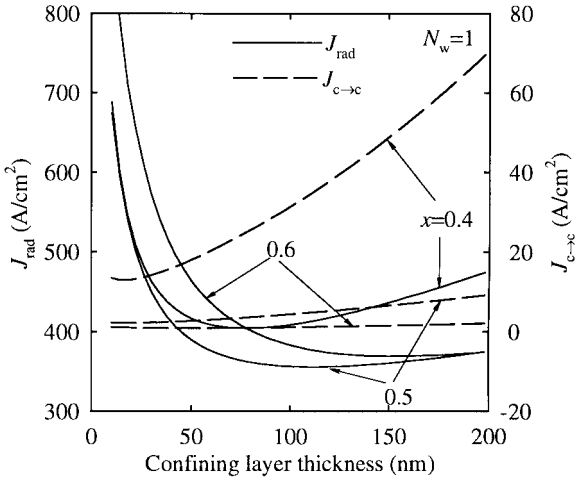

(b)

Fig. 5. (a) The bound-to-bound radiative current density J_{b-b} (the solid lines) and the bound-to-continuum radiative current density J_{b-c} (the dashed lines) and (b) the continuum-to-continuum radiative current density J_{c-c} (the dashed lines) and the total radiative current density $J_{\rm rad}$ (the solid lines) versus the thickness of confining layers for single QW lasers at threshold. Three different Al contents of the $(Al_xGa_{1-x})_{0.5}In_{0.5}P$ confining layers are considered, $x = 0.4,\ 0.5$, and 0.6.

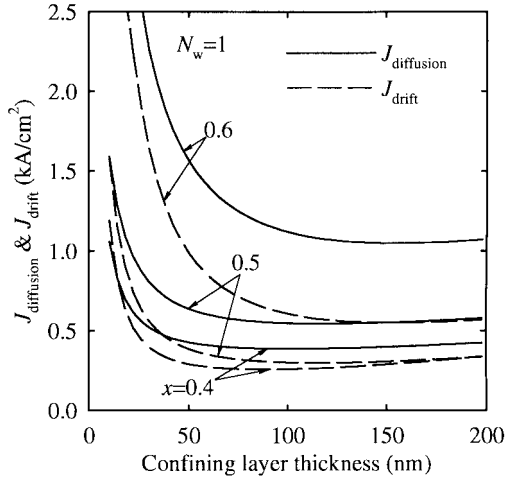

Fig. 6. The diffusion leakage current density $J_{\rm diffusion}$ (the solid lines) and the drift leakage current density $J_{\rm drift}$ (the dashed lines) versus the thickness of confining layers for single QW lasers at threshold. Three different Al contents of the $(Al_xGa_{1-x})_{0.5}In_{0.5}P$ confining layers are considered, $x = 0.4,\ 0.5$, and 0.6.

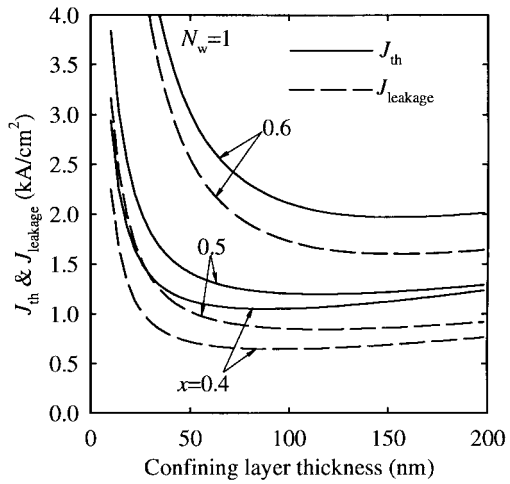

Fig. 7. The total leakage current density $J_{\rm leakage}$ (the dashed lines) and the total threshold current density $J_{\rm th}$ (the solid lines) versus the thickness of confining layers for single QW lasers at threshold. Three different Al contents of the $(Al_xGa_{1-x})_{0.5}In_{0.5}P$ confining layers are considered, $x = 0.4,\ 0.5$, and 0.6.

higher Al content $(x = 0.5)$ confining layers have a lower radiative current than those with $x = 0.4$. This result is quite different from that without considering the optical transition from/to the continuum states [see J_{b-b} in Fig. 5(a)].

Fig. 6 shows the curves for the diffusion current density $J_{\rm diffusion}$ and the drift current density $J_{\rm drift}$ at threshold. As can be seen, $J_{\rm diffusion}$ is higher than $J_{\rm drift}$. In addition, $J_{\rm diffusion}$ and $J_{\rm drift}$ are higher for devices with higher Al confining layers. The diffusion current depends on the electron carrier density $n_{\rm clad}$ in the p-cladding layer, which is related to the quasi-Fermi level separation $E_{\rm fc} - E_{\rm fv}$. For lasers with a high Al content in the confining layers, due to the large separation between quantized levels in the conduction and the valence bands and the high gain required to reach threshold, the quasi-Fermi level separation $E_{\rm fc} - E_{\rm fv}$ is large. Compared with $J_{\rm rad}$ in Fig. 5(b), $J_{\rm drift}$ is comparable to $J_{\rm rad}$. Since $J_{\rm drift}$ depends on $J_{\rm rad}$, as expressed in (42), it increases with the power level and may become serious above threshold. This may result in a poor light–current characteristic if the laser is improperly designed.

Fig. 7 shows the total leakage current density $J_{\rm leakage}$ and the threhsold current density $J_{\rm th}$ as functions of the confining layer thickness for the three Al contents in confining layers. As can be seen, the leakage current is serious and dominates over the radiative current. $J_{\rm leakage}$ is very high for devices with $x = 0.6$, resulting in a very high $J_{\rm th}$. But $J_{\rm th}$ for devices with $x = 0.5$ is slightly higher than that for devices with $x = 0.4$.

The emission wavelengths for devices with different structures are shown in Fig. 8. The emission wavelength depends on the quasi-Fermi level separation $E_{\rm fc} - E_{\rm fv}$ and the bandgap shrinkage energy Δ_{cv}. Since the separation $E_{\rm fc} - E_{\rm fv}$ is larger for higher barriers (having a larger x), the emission wavelength is generally shorter for higher Al content in the confining

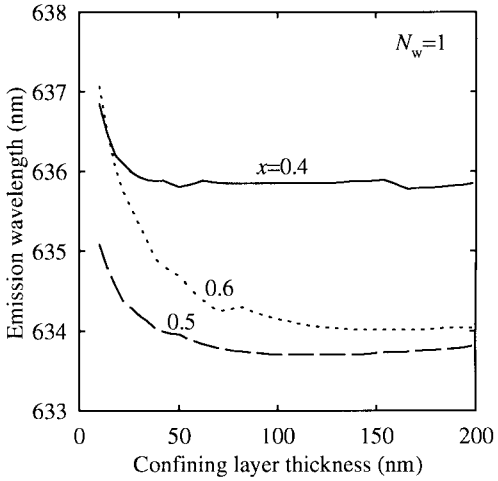

Fig. 8. The emission wavelength versus the thickness of confining layers for single QW lasers at threshold. Three different Al contents of the $(Al_xGa_{1-x})_{0.5}In_{0.5}P$ confining layers are considered, $x = 0.4,\ 0.5$, and 0.6.

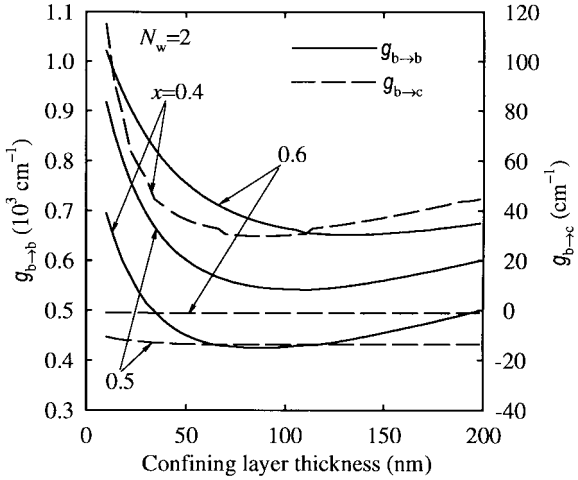

Fig. 9. The bound-to-bound gain g_{b-b} (the solid lines) and the bound-to-continuum gain g_{b-c} (the dashed lines) versus the thickness of confining layers for double QW lasers at threshold. Three different Al contents of the $(Al_xGa_{1-x})_{0.5}In_{0.5}P$ confining layers are considered, $x = 0.4,\ 0.5$, and 0.6.

layers. The effect of the bandgap shrinkage is also important. For example, as the confining layer thickness is small, the emission wavelength is generally red-shifted. This is because higher gains and higher carrier densities are needed to reach the threshold condition, resulting in more serious band gap shrinkage [see (31)]. Another example is that the emission wavelength for $x = 0.5$ is shorter than for $x = 0.6$. This is because the bandgap shrinkage is more serious for $x = 0.6$ although its quasi-Fermi level separation is larger.

According to the above analysis, we can now obtain an optimized single QW laser structure which has 100∼150-nm $(Al_{0.5}Ga_{0.5})_{0.5}In_{0.5}P$ confining layers. The threshold current density is ∼1.3 kA/cm^2 and the emission wavelength is ∼634 nm. Single QW lasers have some drawbacks. They are all caused by the narrow gain region. The narrow gain region gives rise to a small confinement factor and therefore a high gain is needed to reach threshold. The quasi-Fermi level difference $E_{fc} - E_{fv}$ is large and a high leakage current results. In addition, the threshold carrier density is high for such lasers, resulting in serious bandgap shrinkage. An undesired long emission wavelength may be obtained. To obtain a low leakage current and a short emission wavelength, multiple QW lasers with a wide gain region are necessary.

B. Double QW's

In this subsection, we consider lasers with double QW's. The QW thickness is again 80 Å and the barrier sandwiched between the wells is 40 Å. The other parameters are the same as those described before.

Fig. 9 shows the curves for $g_{b\to b}$ and $g_{b\to c}$ at threshold. A remarkable difference between the curves and those shown in Fig. 4 for single QW lasers is that the gain $g_{b\to b}$'s of the double QW lasers are about three times smaller than those of the single QW lasers. This is because the confinement factors for $N_w = 2$ are about three times larger than those for $N_w = 1$. The threshold carrier density in the QW region is therefore greatly reduced and the quasi-Fermi-level separation $E_{fc} - E_{fv}$ becomes small. $g_{b\to c}$'s for $N_w = 2$ are smaller compared with those for $N_w = 1$. This is because the reduced quasi-Fermi-level separation leads to the decrease in the occupation probability difference $f^c_{nk_t} - f^{v\sigma}_{m\nu k_t}$. Similar to the case for $N_w = 1$, $g_{b\to c}$ is much smaller than $g_{b\to b}$, and $g_{c\to b}$ and $g_{c\to c}$ can be totally ignored. So, in general, when calculating the gain, one can actually only consider the $b \to b$ gain.

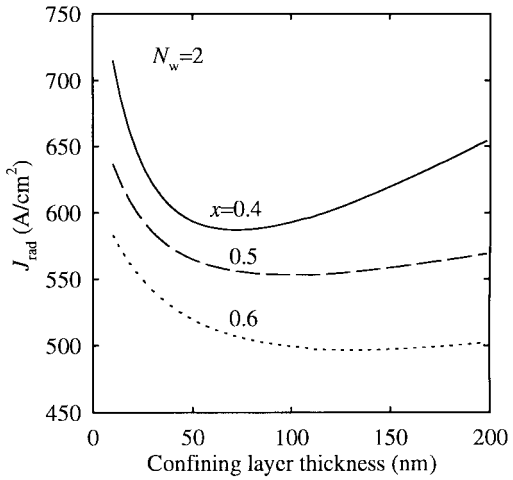

Fig. 10. The total radiative current density J_{rad} versus the thickness of confining layers for double QW lasers at threshold. Three different Al contents of the $(Al_xGa_{1-x})_{0.5}In_{0.5}P$ confining layers are considered, $x = 0.4,\ 0.5$, and 0.6.

For $N_w = 2$, the spontaneous emission rate is lower since the carrier densities are reduced. However, due to the increase in the thickness of the QW region, the radiative current is not expected to have a significant change. The calculted total radiative current densities J_{rad} are shown in Fig. 10. Compared with the curves for $N_w = 1$ shown in Fig. 5(b), the J_{rad} values are typically larger for $N_w = 2$.

Although the radiative current increases, the leakage current is improved significantly. Shown in Fig. 11 is the plot for the diffusion current density $J_{diffusion}$ and the drift current

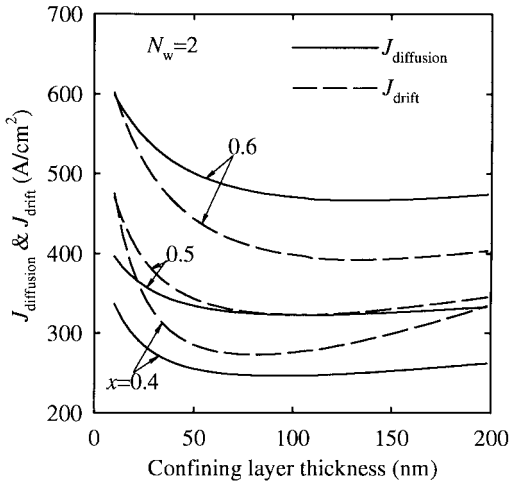

Fig. 11. The diffusion leakage current density $J_{\rm diffusion}$ (the solid lines) and the drift leakage current density $J_{\rm drift}$ (the dashed lines) versus the thickness of confining layers for double QW lasers at threshold. Three different Al contents of the $(Al_xGa_{1-x})_{0.5}In_{0.5}P$ confining layers are considered, $x = 0.4,\ 0.5$, and 0.6.

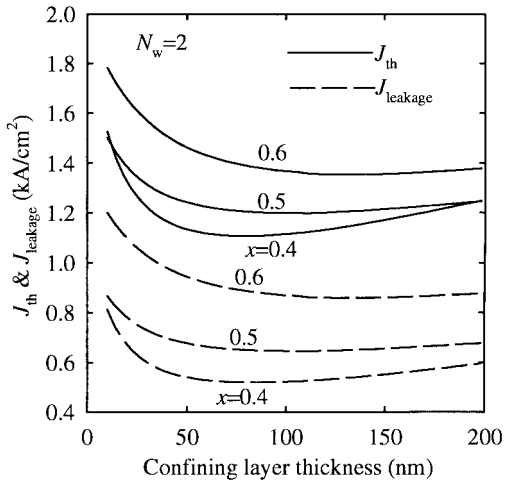

Fig. 12. The total leakage current density $J_{\rm leakage}$ (the dashed lines) and the total threshold current density $J_{\rm th}$ (the solid lines) versus the thickness of confining layers for double QW lasers at threshold. Three different Al contents of the $(Al_xGa_{1-x})_{0.5}In_{0.5}P$ confining layers are considered, $x = 0.4,\ 0.5$, and 0.6.

density $J_{\rm drift}$. Compared with Fig. 6 for $N_w = 1$, $J_{\rm diffusion}$ is reduced considerably, especially for confining layers with high Al content $(x = 0.6)$. $J_{\rm drift}$ is not improved as much as $J_{\rm diffusion}$ since $J_{\rm drift}$ is dependent on $J_{\rm rad}$ which rises when the number of QW's increases. Different from the case for $N_w = 1$ (see Fig. 6), $J_{\rm drift}$ becomes higher than $J_{\rm diffusion}$ for $N_w = 2$. The total leakage current density $J_{\rm leakage}$ and the threshold current density $J_{\rm th}$ are shown in Fig. 11. Compared with Fig. 7 for $N_w = 1$, the leakage current is reduced significantly, especially for large x values. Note that the leakage current still dominates over the radiative current for $x \geq 0.5$ (compared with Fig. 10). The threshold current for $x = 0.6$ is reduced significantly by adding an additional QW. But for low Al content $(x = 0.4{\sim}0.5)$, the threshold currents are not improved very much.

Shown in Fig. 13 is the plot for the emission wavelength. Compared with Fig. 8 for $N_w = 1$, the wavelength becomes shorter for $N_w = 2$. This is because the threshold carrier density in the gain region is reduced. The band gap shrinkage is thus not as serious as that for $N_w = 1$. For $x = 0.5$ and 0.6, the emission wavelength reaches a low value of <632 nm. Different from the case for $N_w = 1$, the emission wavelength for devices with $x = 0.5$ is longer than that for devices with $x = 0.6$. These calculated results are in good agreement with the experimental results. So the effect of bandgap shrinkage is very important while analyzing such a kind of lasers.

Now we can conclude that the optimum structure for $N_w = 2$ is the one with 50~150-nm $(Al_{0.5}Ga_{0.5})_{0.5}In_{0.5}P$ confining layers if the other parameters are kept the same as before. The threshold current density is ~1.2 kA/cm^2 and the emission wavelength is ~632 nm. Comparing the threshold current and the emission wavelength between the optimum structures for $N_w = 1$ and $N_w = 2$, one can find that the double QW laser is superior to the single QW laser since the short wavelength of 632 nm is desirable.

Further increasing the QW number does not significantly improve the threshold current and the emission wavelength.

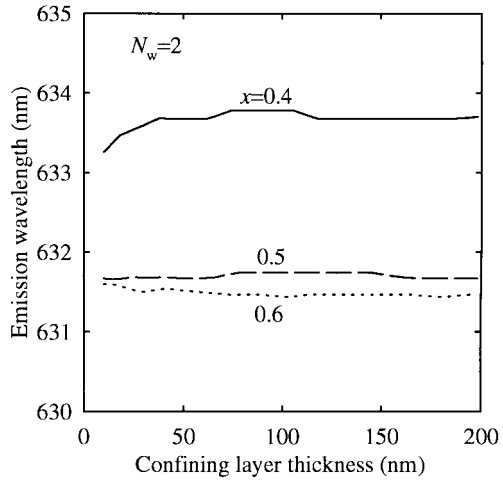

Fig. 13. The emission wavelength versus the thickness of confining layers for double QW lasers at threshold. Three different Al contents of the $(Al_xGa_{1-x})_{0.5}In_{0.5}P$ confining layers are considered, $x = 0.4,\ 0.5$, and 0.6.

We have studied the triple QW lasers. The results showed that the radiative current densities are typically ~650 A/cm^2 for both $x = 0.5$ and 0.6. The diffusion current is slightly improved but the drift current basically remains the same as that for $N_w = 2$. As a result, the threshold current becomes slightly lower for $x = 0.6$ but slightly higher for $x = 0.5$, compared with the threshold current for $N_w = 2$. The emission wavelength for $x = 0.5$ is slightly longer (~632 nm) but slightly shorter for $x = 0.6$ (~631.2 nm) than the wavelength for $N_w = 2$.

C. Dopant Concentration in p-Cladding Layer

From the previous analysis, one can find that the leakage current is still high for double QW lasers. In fact, due to the inherent limitation of available material for such lasers, the leakage current is sensitively dependent on the doping

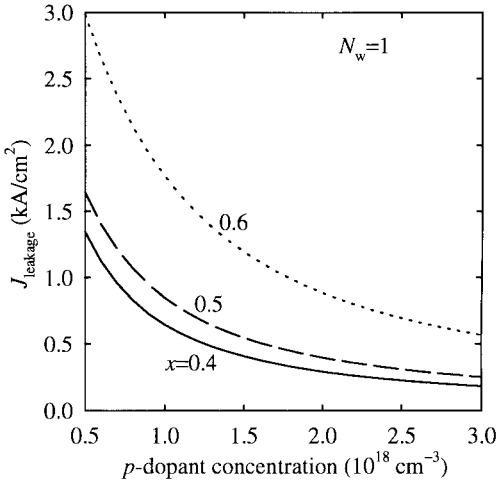

Fig. 14. The total leakage current density J_{leakage} versus the dopant concentration in the p-cladding layer for single QW lasers at threshold. Three different Al contents of the $(Al_xGa_{1-x})_{0.5}In_{0.5}P$ confining layers are considered, $x = 0.4,\ 0.5$, and 0.6.

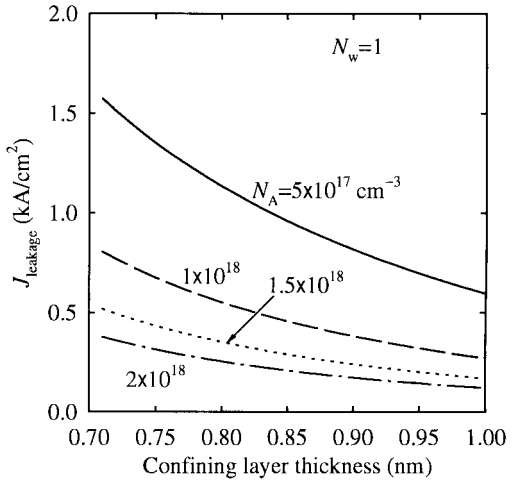

Fig. 15. The total leakage current density J_{leakage} versus the Al content of the $(Al_xGa_{1-x})_{0.5}In_{0.5}P$ cladding layers for single QW lasers at threshold. Four different dopant concentrations in the p-cladding layer are considered, N_A = 0.5, 1, 1.5, and 2×10^{18} cm^{-3}.

concentration in the p-cladding layer. For a higher p-dopant concentration, the quasi-Fermi levels E_{fc} and E_{fv} are both closer to the valence band. As a result, the electron density is reduced and the hole density rises. The diffusion and the drift currents are therefore reduced. Fig. 14 shows the leakage current density at threshold as a function of the dopant concentration of the p-cladding layer for single QW lasers. Three Al contents of confining layers are considered, $x = 0.4, 0.5$, and 0.6. The confining layer thickness is taken to be 100 nm. As can be seen, the leakage current is very sensitive to the dopant concentration when the doping concentration $<1.5\times10^{18}$ cm^{-3}. The improvement on the leakage current is effective by increasing the dopant in the p-cladding layer. So, the dopant concentration should be as high as possible. However, in reality, it is difficult to obtain a very high p-doping concentration in $(Al_xGa_{1-x})_{0.5}In_{0.5}P$ with $x > 0.7$.

D. Al Content of Cladding Layers

To further reduce the leakage current density, one can utilize the cladding layers with a higher Al content. A higher Al content in cladding layers gives rise to two advantages. Since the band gap becomes wider, the leakage of the minority carrier is suppressed. In addition, the refractive-index difference between the cladding and the confining layers is larger, and the optical mode is more tightly confined so the confinement factor becomes larger. This results in a lower threshold gain and a reduced separation of the quasi-Fermi levels, which again reduces the leakage current. Fig. 15 shows the leakage current density at threshold versus the Al content of cladding layers for different p-doping concentrations. The lasers have a single QW. The Al content and the thickness of confining layers are taken to be $x = 0.5$ and 100 nm, respectively. The cavity length is still assumed to be 500 μm. It can be seen from the figure that the leakage current is reduced considerably by increasing the Al content in the cladding layers with a low doping concentration. Low leakage current can therefore be obtained by using the AlInP cladding layers with a high dopant density. Our calculation shows that a low threshold current density of 620 A/cm^2 can be obtained for lasers with AlInP cladding layers with $N_A = 1\times10^{18}$ cm^{-3}. This result is consistent with the observation [7]. However, in practice, the high-Al cladding layers may cause other problems. Heavily p-doped cladding layers are difficult to be obtained as the Al content increases. Additionally, tight confinement of the optical mode may lead to a poor beam divergence. These problems have to be considered in designing the lasers.

IV. Conclusion

We have theoretically analyzed in detail the 630-nm GaInP–AlGaInP tensile-strained QW lasers. The 6×6 Luttinger–Kohn Hamiltonian has been used for calculating the valence band structure including the coupling effect of spin-orbital split-off bands. The effect of the optical transitions from/to the continuum states has also been taken into account. The results show that although the gains due to the optical transitions from/to the continuum states are small compared to the gain due to the bound-to-bound transition, the radiative currents arising from the optical transitions from/to the continuum states are significant and cannot be neglected. To avoid unreasonable absorption below the band gap, a more practical lineshape function, the non-Markovian lineshape, should be adopted for gain calculation. It has been shown that the use of such lineshape is very important for the correct gain calculation. The band-gap shrinkage effect due to carrier-carrier interaction has been considered. The results indicate that the bandgap-shrinkage effect plays an important role in obtaining a correct emission wavelength.

The problem of leakage current is serious for single QW lasers. It can be improved by increasing the QW number, the p-cladding layer dopant concentration, and the band gap of the cladding layers. We have optimized the laser structures to achieve a low threshold current and a short emission wavelength. For single QW lasers with $(Al_{0.7}Ga_{0.3})_{0.5}In_{0.5}P$ cladding layers, the optimized confining layers have been

found to be 100∼150-nm $(Al_{0.5}Ga_{0.5})_{0.5}In_{0.5}P$. The calculated threshold current density is ∼1.3 kA/cm^2 and the emission wavelength is ∼634 nm for a 500-μm-long cavity. For double QW lasers, the optimized confining layers are 50∼150-nm $(Al_{0.5}Ga_{0.5})_{0.5}In_{0.5}P$. The corresponding threshold current density is ∼1.2 kA/cm^2 and the emission wavelength is ∼632 nm for a 500-μm-long cavity. The double QW laser is preferred due to its shorter emission wavelength. Further increasing the QW number does not make significantly improvement on the threshold current and the emission wavelength.

APPENDIX

The polarization dependent matrix elements in (23)–(28) are derived in this appendix. Based on Kane's theory [37], the wave functions with small vector k's have the following set of transformed cell-periodic functions for the effective hamiltonian $\bar{H}^{\sigma}_{3\times3}$ in (12):

$$|(\sigma,1)'\rangle = \frac{1}{2}\big[-|(X'+iY')\uparrow'\rangle e^{-i\frac{3}{2}\phi'} \mp i|(X'-iY')\downarrow'\rangle e^{i\frac{3}{2}\phi'}\big] \tag{A1}$$

$$|(\sigma,2)'\rangle = \frac{1}{2\sqrt{3}}\big[-|(X'-iY')\uparrow' + 2Z'\downarrow'\rangle e^{i\frac{1}{2}\phi'} \pm i|-(X'+iY')\downarrow' + 2Z'\uparrow'\rangle e^{-i\frac{1}{2}\phi'}\big] \tag{A2}$$

$$|(\sigma,3)'\rangle = \frac{1}{\sqrt{6}}\big[-|(X'-iY')\uparrow' - Z'\downarrow'\rangle e^{i\frac{1}{2}\phi'} \mp i|(X'+iY')\downarrow + Z'\uparrow\rangle e^{-i\frac{1}{2}\phi'}\big] \tag{A3}$$

where $\sigma = U$ (or L) is the index for the upper (lower) signs. The transformed S', X', Y', and Z' are related to S, X, Y, and Z at $k = 0$ by

$$\begin{bmatrix} X' \\ Y' \\ Z' \end{bmatrix} = \begin{bmatrix} \cos\theta\cos\phi & \cos\theta\sin\phi & -\sin\theta \\ -\sin\phi & \cos\phi & 0 \\ \sin\theta\cos\phi & \sin\theta\sin\phi & \cos\theta \end{bmatrix} \begin{bmatrix} X \\ Y \\ Z \end{bmatrix} \tag{A4}$$

$$S' = S. \tag{A5}$$

where $\theta = \cos^{-1}(k_z/k)$ and $\phi = \tan^{-1}(k_x/k_y)$. The transformation is taken so that the new z' axis is along the wave vector k. Using the basis functions (A1)–(A3) and relation (A4), the squared momentum matrix element

$$\begin{aligned} &\left|\hat{x}\cdot\mathbf{M}^{\eta\sigma}_{nm,\nu=1}(k_t)\right|^2 \\ &\quad= \left|\langle\bar{\Psi}^{v\sigma}_{m,\nu=1,k_t}|p_x|\Phi^{c\eta}_{nk_t}\rangle\right|^2 \\ &\quad= \left|\langle(\sigma,1)'|p_x|S'\eta'\rangle\right|^2\left|\langle\bar{\psi}^{v\sigma}_{m,\nu=1,k_t}|\phi^{c}_{nk_t}\rangle\right|^2 \\ &\quad= \frac{1}{4}\left|\langle S|p_x|X\rangle\right|^2(\cos^2\theta\cos^2\phi+\sin^2\phi) \\ &\qquad\times\left|\langle\bar{\psi}^{v\sigma}_{m,\nu=1,k_t}|\phi^{c}_{nk_t}\rangle\right|^2. \end{aligned} \tag{A6}$$

Taking average over ϕ and using (25), we have

$$\left|\hat{x}\cdot\mathbf{M}^{\eta\sigma}_{nm,\nu=1}(k_t)\right|^2 = \frac{3}{8}M_b^2(1+\cos^2\theta)\left|\langle\bar{\psi}^{v\sigma}_{m,\nu=1,k_t}\mid\phi^{c}_{nk_t}\rangle\right|^2 \tag{A7}$$

which is just the squared momentum matrix element in (23). The average over ϕ is associated with the axial approximation of the band structure in the gain calculation.

Similarly, the other squared matrix elements in (24)–(28) can also be deduced by the same procedure.

REFERENCES

[1] A. Valster, C. J. Van Der Poel, M. N. Finke, and M. J. B. Boermans, "Effect of strain on the threshold current of GaInP/AlGaInP quantum well lasers emitting at 633 nm," in *Tech. Dig. 13th IEEE Int. Semiconductor Laser Conf.*, Takamatsu, Japan, 1992, paper G1.

[2] P. Blood and P. M. Smowton, "Strain dependence of threshold current in fixed-wavelength GaInP laser diodes," *IEEE J. Select. Topics Quantum Electron.*, vol. 1, pp. 707–711, 1995.

[3] D. Ahn, S. J. Yoon, S. L. Chuang, and C. S. Chang, "Theory of optical gain in strained-layer quantum wells within the 6×6 Luttinger–Kohn model," *J. Appl. Phys.*, vol. 78, pp. 2489–2497, 1995.

[4] G. Hatakoshi, K. Itaya, M. Ishikawa, M. Okajima, and Y. Uematsu, "Short-wavelength InGaAlP visible laser diodes," *IEEE J. Quantum Electron.*, vol. 27, pp. 1476–1482, 1991.

[5] H. Hamada, S. Honda, M. Shono, R. Hiroyama, K. Yodoshi, and T. Yamaguchi, "Activation of Zn acceptors in AlGaInP epitaxial layers grown on misoriented substrates by metal organic chemical vapor deposition," *Electron. Lett.*, vol. 28, pp. 585–587, 1992.

[6] G. Hatakoshi, K. Nitta, K. Itaya, Y. Nishikawa, M. Ishikawa, and M. Okajima, "High-power InGaAlP laser diodes for high-density optical recording," *Jpn. J. Appl. Phys.*, vol. 31, pp. 501–507, 1992.

[7] D. P. Bour, D. W. Treat, R. L. Thornton, T. L. Paoli, R. D. Bringans, B. S. Krusor, R. S. Geel, D. F. Welch, and T. Y. Wang, "High-power InGaAlP laser diodes for high-density optical recording," *J. Crystal Growth*, vol. 124, pp. 751–756, 1992.

[8] I. Nomura, K. Kishino, A. Kikuchi, and Y. Kaneko, "600-nm-range GaInP/AlInP strained quantum well lasers grown by gas source molecular beam epitaxy," *Jpn. J. Appl. Phys.*, vol. 33, pp. 804–810, 1994.

[9] S. Kamiyama, M. Monnoh, K. Ohnaka, and T. Uenoyama, "Studies of threshold current dependence on compressive and tensile strain of 630 nm GaInP/AlGaInP multi-quantum-well lasers," *J. Appl. Phys.*, vol. 75, pp. 8201–8203, 1994.

[10] S. Kamiyama, T. Uenoyama, M. Monnoh, and K. Ohnaka, "Theoretical studies of GaInP–AlGaInP strained quantum-well lasers including spin-orbit split-off band effect," *IEEE J. Quantum Electron.*, vol. 31, pp. 1409–1417, 1995.

[11] A. T. Meney, A. D. Prins, A. F. Phillips, J. L. Sly, E. P. O'Reilly, D. J. Dunstan, A. R. Adams, and A. Valster, "Determination of the band structure of disordered AlGaInP and its influence on visible-laser characteristics," *IEEE J. Select. Topics Quantum Electron.*, vol. 1, pp. 697–706, 1995.

[12] C. Y.-P. Chao and S. L. Chuang, "Spin-orbit-coupling effects on the valence-band structure of strained semiconductor quantum wells," *Phys. Rev. B*, vol. 46, pp. 4110–4122, 1992.

[13] C. S. Chang and S. L. Chuang, "Modeling of strained quantum-well lasers with spin-orbital coupling," *IEEE J. Select. Topics Quantum Electron.*, vol. 1, pp. 218–229, 1995.

[14] M. Yamanishi and Y. Lee, "Phase dampings of optical dipole moments and gain spectra in semiconductor lasers," *IEEE J. Quantum Electron.*, vol. QE-23, pp. 367–370, 1987.

[15] T. Ohtoshi and M. Yamanishi, "Optical line shape functions in quantum-well and quantum-wire structures," *IEEE Quantum Electron.*, vol. 27, pp. 46–53, 1991.

[16] M. Asada, "Intraband relaxation effect on optical spectra," in *Quantum Well Lasers*, P. S. Zory Jr., Ed. San Diego, CA: Academic, 1993, pp. 97–130.

[17] A. D. Prins, J. L. Sly, A. T. Meney, D. J. Dunstan, E. P. O'Reilly, A. R. Adams, and A. Valster, "High pressure determination of AlGaInP band structure," *J. Phys. Chem. Solids*, vol. 56, pp. 349–352, 1995.

[18] ——, "Direct measurement of band offsets in GaInP/AlGaInP using high pressure," *J. Phys. Chem. Solids*, vol. 56, pp. 423–427, 1995.

[19] H. Hirayama, Y. Miyake, and M. Asada, "Analysis of current injection efficiency of separate-confinement-heterostructure quantum-film lasers," *IEEE J. Quantum Electron.*, vol. 28, pp. 68–74, 1992.

[20] J. Lee, M. O. Vassell, and G. J. Jan, "Energy-band diagrams of P-i-N heterostructures for single quantum-well lasers," *IEEE J. Quantum Electron.*, vol. 29, pp. 1469–1476, 1993.

[21] Z. Ikonic, V. Milanovic, and D. Tjakin, "Bound-free intraband absorption in GaAs-$Al_x Ga_{1-x}$As semiconductor quantum wells," *Appl. Phys. Lett.*, vol. 54, pp. 247–249, 1989.

[22] S. R. Chinn, P. S. Zory, and A. R. Reisinger, "A model for GRIN-SCH-SQW diode lasers," *IEEE J. Quantum Electron.*, vol. 24, pp. 2191–2214, 1988.

[23] M. Yamanishi and I. Suemune, "Comment on polarization dependent momentum matrix elements in quantum well lasers," *Jpn. J. Appl. Phys.*, vol. 29, pp. 1469–1476, 1993.
[24] M. Asada, A. Kameyama, and Y. Suematsu, "Gain and intervalence band absorption in quantum-well lasers," *IEEE J. Quantum Electron.*, vol. QE-20, pp. 745–753, 1984.
[25] M. Yamada, S. Orgita, M. Yamagishi, and K. Tabata, "Anisotropy and broadening of optical gain in a GaAs/AlGaAs multi-quantum well laser," *IEEE J. Quantum Electron.*, vol. QE-21, pp. 640–645, 1985.
[26] J. Camassel, D. Auvergne, and H. Mathieu, "Temperature dependence of the band gap and comparison with the threshold frequency of pure GaAs lasers," *J. Appl. Phys.*, vol. 46, pp. 2683–2689, 1975.
[27] H. Kressel and J. K. Butler, *Semiconductor Lasers and Heterojuction LEDs*. New York: Academic, 1977, p. 91.
[28] D. A. Kleinman and R. C. Miller, "Band-gap renormalization in semiconductor quantum wells containing carriers," *Phys. Rev. B*, vol. 32, pp. 2266–2272, 1985.
[29] H. C. Casey, Jr., and M. B. Panish, *Heterostructure Lasers*. New York: Academic, 1978, pt. A, pp. 248–253.
[30] M. D. Dawson and G. Duggan, "Band-offset determination for GaInP-AlGaInP structures with compressively strained quantum well active layers," *Appl. Phys. Lett.*, vol. 64, pp. 892–894, 1994.
[31] D. J. Mowbray, O. P. Kowalski, M. Hopkinson, M. S. Skolnick, and J. P. R. David, "Electronic band structure of AlGaInP grown by solid source molecular beam epitaxy," *Appl. Phys. Lett.*, vol. 65, pp. 213–215, 1994.
[32] M. D. Dawson, G. Duggan, and D. J. Arent, "Optical measurements of electronic bandstructure in tensile strain GaInP-AlGaInP quantum wells," *Phys. Rev. B*, vol. 51, pp. 17660–17666, 1995.
[33] H. K. Yow, P. A. Houston, and M. Hopkinson, "Conduction band discontinuities in $Ga_{0.5}In_{0.5}P$–$Al_xGa_{0.5-x}In_{0.5}P$ heterojunctions measured by internal photoemission," *Appl. Phys. Lett.*, vol. 66, pp. 2852–2854, 1995.
[34] S. P. Najda, A. H. Kean, M. D. Dawson, and G. Duggan, "Optical measurements of electronic bandstructure in AlGaInP alloys grown by gas source molecular beam epitaxy," *J. Appl. Phys.*, vol. 77, pp. 3412–3415, 1995.
[35] D. P. Bour, "AlGaInP quantum well lasers," in *Quantum Well Lasers*, P. S. Zory, Jr., Ed. San Diego, CA: Academic, 1993, pp. 415–460.
[36] U. Strauss, W. W. Rühle, H. J. Queisser, K. Nakano, and A. Ishibashi, "Band-to-band recombination in $Ga_{0.5}In_{0.5}P$," *J. Appl. Phys.*, vol. 75, pp. 8204–8206, 1994.
[37] E. O. Kane, "Band structure of indium antimonide," *J. Phys. Chem. Solids*, vol. 1, pp. 249–261, 1957.

Shun Tung Yen, photograph and biography not available at the time of publication.

Chien-Ping Lee (M'80–SM'94), photograph and biography not available at the time of publication.